Non-MHD effects in the nonlinear development of the MHD-scale Rayleigh-Taylor instability

Takayuki Umeda, and Yasutaka Wada

Citation: Physics of Plasmas **24**, 072307 (2017);
View online: https://doi.org/10.1063/1.4991409
View Table of Contents: http://aip.scitation.org/toc/php/24/7
Published by the American Institute of Physics

Non-MHD effects in the nonlinear development of the MHD-scale Rayleigh-Taylor instability

Takayuki Umeda[a] and Yasutaka Wada
Institute for Space-Earth Environmental Research, Nagoya University, Nagoya 464-8601, Japan

(Received 17 January 2017; accepted 20 June 2017; published online 7 July 2017)

The nonlinear evolution of the Rayleigh-Taylor instability (RTI) at a density shear layer transverse to magnetic field in a collisionless plasma is investigated by means of a fully kinetic Vlasov simulation with two spatial and two velocity dimensions. The primary RTI in the MHD regime develops symmetrically in a coordinate axis parallel to gravity as seen in the previous MHD simulations. The primary RTI in the Hall-MHD regime develops asymmetrically in a coordinate axis parallel to gravity. A compressible flow is formed at the secondary density shear layer by the Hall effect, which generates a strong scalar pressure gradient of ions. A Hall electric field due to the diamagnetic current results in the asymmetric flow at the tip of the finger structure. In the primary RTI with the ion gyro kinetic effect, secondary RTI with a wavelength shorter than the wavelength of the primary RTI is generated at the saturation stage of the primary RTI. A seed perturbation for the secondary RTI is excited by another secondary instability due to the coupling between the electron stress tensor and the Hall electric field. The heat flux term plays an important role in the time development of the total pressure. On the other hand, the contribution of the ion stress tensor is small in both the electric current and the total pressure. *Published by AIP Publishing.* [http://dx.doi.org/10.1063/1.4991409]

I. INTRODUCTION

The Rayleigh-Taylor instability (RTI) is a well-known hydrodynamic instability in neutral fluid as well as in magnetized plasma, which grows at an interface between two fluids when a light fluid supports a heavy fluid against an external force such as gravity. It has been known from (neutral) hydrodynamic simulations that the interface develops as rising bubbles of the light fluid between falling spikes (known as finger/mushroom structures) of the heavy fluid. The primary RTI takes place in various situations in natural plasma, such as in the atmosphere/ionosphere of stars/planets due to gravity. The RTI is also generated as a secondary instability of the Kelvin-Helmholtz instability (KHI) due to a centrifugal force.[1,2]

The previous magneto-hydro-dynamic (MHD) simulations have shown that the development of the RTI transverse to the ambient magnetic field in collisionless magnetized plasma is similar to that in the neutral fluid.[3–5] The bubble and finger/mushroom structures formed by the RTI develop symmetrically in a coordinate axis parallel to gravity.

Numerical simulations of the RTI with non-MHD effects have been performed by using the Hall MHD code,[6–9] the Finite-Larmor-Radius (FLR) MHD code,[8–10] and the hybrid particle-in-cell (PIC) code.[11,12] In these previous simulations, it has been shown that the RTI develops asymmetrically in a coordinate axis parallel to gravity due to "non-MHD" effects. In the previous simulation studies with non-MHD effects, however, turbulent mixing of multiple RT modes makes it difficult to identify non-MHD processes on the asymmetric development of the RTI in the nonlinear stage. This is because multiple wave modes with random phases are imposed as an initial perturbation in extended MHD simulations and multiple RT modes grow from thermal noises/fluctuations due to a finite number of particles in hybrid simulations.

"What are non-MHD effects?" is an open question in plasma physics. Most plasma physicists believe that the ion inertial (Hall) effect plays a role when the spatial scale of a phenomenon is close to the ion inertial length and that the ion gyro kinetic effect plays a role when the spatial scale of a phenomenon is close to the ion gyro radius. A purpose of the present study is to separate non-MHD effects from purely ideal MHD effects in the *nonlinear* development of the RTI. For this purpose, we impose a single wave mode as an initial perturbation in a full kinetic simulation by using a Vlasov code. We perform several simulation runs with different plasma beta values by varying the ratio of the ion inertial length or the ion gyro radius to the spatial scale of the RTI in order to identify the Hall effect and the ion gyro kinetic effect especially.

II. VLASOV SIMULATION SETUP

The Vlasov code used in the present study solves the Vlasov equation (1) together with the Maxwell equations (2) in two spatial and two velocity dimensions (x,y,v_x,v_y), which has already been used for studies of the KHI[13–15] and the RTI[16]

$$\frac{\partial f}{\partial t}+\boldsymbol{v}\cdot\frac{\partial f}{\partial \boldsymbol{x}}+\frac{q}{m}(\boldsymbol{E}+\boldsymbol{v}\times\boldsymbol{B})\cdot\frac{\partial f}{\partial \boldsymbol{v}}=0, \tag{1}$$

[a]Email: taka.umeda@nagoya-u.jp

$$\left.\begin{aligned} \frac{1}{c^2}\frac{\partial \boldsymbol{E}}{\partial t} - \nabla \times \boldsymbol{B} + \mu_0 \boldsymbol{J} = 0 \\ \frac{\partial \boldsymbol{B}}{\partial t} + \nabla \times \boldsymbol{E} = 0 \\ \nabla \cdot \boldsymbol{E} - \frac{\rho}{\epsilon_0} = 0 \\ \nabla \cdot \boldsymbol{B} = 0 \end{aligned}\right\}. \tag{2}$$

The code adopts a non-oscillatory and conservative semi-Lagrangian scheme[17,18] with several improvements[19,20] for solving the Vlasov equation (1), which exactly satisfies the continuity equation for charge,

$$\frac{\partial \rho}{\partial t} + \nabla \cdot \boldsymbol{J} = 0. \tag{3}$$

The Maxwell equations are solved with an implicit version of the Finite-Difference-Time-Domain (FDTD) method.[21] The code is well parallelized and its performance is tuned for recent supercomputers.[22] The detailed descriptions of the simulation code are given in the references.

In the previous (extended-)MHD simulations,[7–10] the initial density shear layer was in the state of the one-dimensional MHD equilibrium. The previous hybrid PIC simulations used a discontinuous density layer with a step function, which is not in an equilibrium state.[11,12] The initial condition of the present study is identical to our previous Vlasov simulation,[16] which satisfies one-dimensional time-independent (steady-state) two-fluid equations for ions and electrons. It is important to use a "stable" initial condition in order to maintain the initial density shear layer for a long simulation time, since we perform Vlasov simulation runs on several hundreds of ion gyro period with a time step on the electron plasma period.

Let us consider a four-dimensional phase space with two spatial and two velocity dimensions (x,y,v_x,v_y) and the gravity in the y direction. In the present coordinate system, the out-of-plane electric field E_z component and the in-plane magnetic field B_x and B_y components are not considered since the out-of-plane current J_z component does not exist. Here, we consider a one-dimensional equilibrium for a density shear layer in which all the physical quantities depend only on the y coordinate. Then, the time-independent two-fluid equations for ions and electrons are written as follows:

$$\frac{\partial P_e}{\partial y} - eN_e(B_z U_{xe} + E_y) = m_e N_e g_y, \tag{4}$$

$$\frac{\partial P_i}{\partial y} + eN_i(B_z U_{xi} + E_y) = m_i N_i g_y, \tag{5}$$

$$\frac{\partial E_y}{\partial y} = \frac{e}{\epsilon_0}(N_i - N_e), \tag{6}$$

$$\frac{\partial B_z}{\partial y} = e\mu_0(N_i U_{xi} - N_e U_{xe}), \tag{7}$$

where U_x represents the bulk velocity of fluids in the x direction.

A two-fluid equilibrium is given with the following assumptions: $N_i = N_e(\equiv N)$, $\partial \beta_{i,e}/\partial y = 0$ (where $\beta_{i,e} = 2\mu_0 P_{i,e}/B_z^2 = 2\omega_{pi,e}^2 V_{ti,e}^2/(c^2\omega_{ci,e}^2)$ with V_t being the thermal velocity), and

$$N[y] = \frac{N_I - N_{II}}{2}\tanh\left[\frac{y}{L}\right] + \frac{N_I + N_{II}}{2}, \tag{8}$$

where L represents the half thickness of the density shear layer. The subscripts I and II represent the upper and lower boundaries, respectively. Solving for P, B_z, and U_x, we obtain

$$P_s[y] = \frac{(m_e + m_i)\beta_s g_y}{\beta_i + \beta_e + 1}\left\{\frac{N_I - N_{II}}{2}\log\left[e^{\frac{y}{L}} + e^{-\frac{y}{L}}\right] + \frac{N_I + N_{II}}{2}y\right\} + P_{0s}, \tag{9}$$

$$B_z[y] = \sqrt{\frac{2\mu_0 P_i[y]}{\beta_i}} = \sqrt{\frac{2\mu_0 P_e[y]}{\beta_e}}, \tag{10}$$

$$U_{xi}[y] = \frac{g_y}{eB_z[y]}\left\{m_i - \frac{(m_e + m_i)\beta_i}{\beta_i + \beta_e + 1}\right\}, \tag{11}$$

$$U_{xe}[y] = -\frac{g_y}{eB_z[y]}\left\{m_e - \frac{(m_e + m_i)\beta_e}{\beta_i + \beta_e + 1}\right\}. \tag{12}$$

Here, P_0 is an integral constant which is determined such that the pressure corresponds to P_I at the upper boundary.

In the present study, we assume that $N_I/N_{II} = 9$. The simulation system is taken for $0 \le x \le 3L$ and $-6L \le y \le 6L$ with $N_x \times N_y = 400 \times 1600$ grid points. Thus, the grid spacing in the configuration space is $\Delta = 0.0075L = 4\lambda_{Di,I}$ for both x and y directions. The velocity space is taken for $-20V_{ti,e,I} \le v_{x,y,i,e} \le 20V_{ti,e,I}$ for both ions and electrons, with $N_{vx} \times N_{vy} = 100 \times 100$ grid points. Thus, the grid spacing in the velocity space is $\Delta v_{i,e} = 0.4V_{ti,e,I}$. It should be noted that we adopt a reduced ion-to-electron mass ratio $m_i/m_e = 25$ for computational efficiency. The periodic boundary condition is imposed in the x direction, while the physical quantities are fixed to their initial values at the boundaries in the y direction.

In contrast to hybrid and full PIC simulations where instabilities grow from thermal noises/fluctuations due to a finite number of particles, Vlasov simulations need a seed perturbation to initiate instabilities as fluid simulations do. In the previous MHD simulations, multiple wave modes with random phases are imposed as an initial perturbation. On the other hand, we impose a single wave mode as an initial perturbation

$$\delta U_{yi,e}[x,y] = U_0 \frac{\cos[k_x x]}{\cosh^2\left[\frac{y}{L}\right]} \tag{13}$$

with $U_0 = 0.01B_{z,I}/\sqrt{\mu_0 m_i N_I}$ and $k_x = 2\pi/(3L)$ (Mode 1).

We perform three different simulation runs with different plasma beta values, as listed in Table I. As seen, we vary the ratio of the half thickness of the initial density shear layer to the ion inertial length (d_i) and the ion thermal gyro radius (r_i) at $y = 0$. The wavelength of the primary RT mode is

TABLE I. Simulation parameters for different simulation runs.

Run	$\beta_{i,e}$	$d_i\|_{y=0}$	$r_i\|_{y=0}$	$g_y/(\omega_{pi,I}V_{ti,I})$	$\omega_{ci,I}/\omega_{pi,I}$	$\omega_{pi,I}\Delta t$
1	1/8	$L/4$	$L/16$	−0.001575	0.002	0.005
2	1/128	L	$L/16$	−0.02075	0.002	0.005
3	2	$L/4$	$L/4$	−0.0004	0.0005	0.02

$\lambda_{RT}(=3L)=12d_i=48r_i$ in Run 1, $\lambda_{RT}=3d_i=48r_i$ in Run 2, and $\lambda_{RT}=12d_i=12r_i$ in Run 3 at $y=0$.

The spatial scale of boundary layers between the high-density and low-density regions becomes smaller as the RTI develops nonlinearly. Then, non-MHD effects are expected to play a role in the nonlinear development of the RTI. Our previous study showed that both the Hall effect and the ion gyro kinetic effect are small on the nonlinear development of the primary RTI in Run 1.[16] Since the ion inertial length in Run 2 is four times as long as that of that in Run 1, it is expected that the Hall effect plays a role in the nonlinear stage of Run 2. Since the ion gyro radius in Run 3 is four times as long as of that in Run 1, it is expected that the ion gyro kinetic effect plays a role in the nonlinear stage of Run 3. It should be noted that the *linear* growth rate can be modified by non-MHD effects, which is, however, not a scope of the present study. The linear growth of the primary RTI is in the MHD regime in the present simulation runs as we show later.

The initial spatial profiles of N, B_z, $P=(P_i+P_e)$, and $U_{xi,e}$ as functions of y are shown in Fig. 1. Here, $B_{z,I}=\sqrt{2\mu_0 P_{s,I}/\beta_s}$. The initial profiles of N, B_z, and P are common when these quantities are normalized by N_I, $B_{z,I}$, and P_I, respectively. On the other hand, the initial profile of the ion and electron bulk velocities depends on the plasma beta, as indicated by Eqs. (11) and (12).

The initial bulk velocities of the MHD fluid U_x in the previous (extended-)MHD simulations[7–10] were assumed to be zero since the MHD equilibrium can take an arbitrary bulk velocity for density shear layers. The initial bulk velocity of ions in the previous hybrid simulations[11,12] was neglected because of the step-like sharp gradient of the density shear layer on the spatial grid scale. On the other hand, the initial bulk velocities of ions and electrons in full kinetic simulations are non-zero due to the $\boldsymbol{g}\times\boldsymbol{B}$ drift and the diamagnetic drift. The initial velocity distributions of the ions and electrons for the present Vlasov simulation are isotropic Maxwellian with the bulk (drift) velocity $U_{xi,e}[y]$ and the thermal velocity $V_{ti,e}[y]\equiv\sqrt{P_{i,e}[y]/mN[y]}$. It should be noted, therefore, that the present initial condition is not a Vlasov equilibrium.

III. SIMULATION RESULT

Figure 2 shows the spatial profiles of ion density at different times in Runs 1–3. The RTI develops symmetrically in a coordinate axis parallel to gravity in Run 1, and typical bubble and finger/mushroom structures are formed as seen in the previous MHD simulations. Secondary instabilities are generated at the right-hand side of the finger/mushroom structure at $t\omega_0=6.5$ and at the upper edge of the bubble at $t\omega_0=7.2$ (where $\omega_0\equiv\sqrt{g_y/L}\sim\omega_{ciI}/23.3$ in Run 1), but these instabilities have been analyzed in our previous study[16] and are not focused on here.

The time development of the RTI in Run 2 is similar to that in Run 1 until $t\omega_0=5.0$ (where $\omega_0\sim\omega_{ciI}/6.4$). The tip of the finger/mushroom structure turns to the right ($+x$ direction) at $t\omega_0=5.0$. Then, a vortex with counter-clockwise rotation is formed. It is noted that similar vortices with counter-clockwise rotation are also seen in the previous Hall-(FLR-)MHD simulation (see Fig. 8 in Ref. 12).

In Run 3, a smaller-scale fluctuation is generated at the interface between the high-density and the low-density regions at $t\omega_0=4.0$ (where $\omega_0\sim\omega_{ciI}/11.5$). It is noted that similar small-scale structures are also seen in the previous hybrid PIC simulation (see Fig. 17 in Ref. 12). These small-

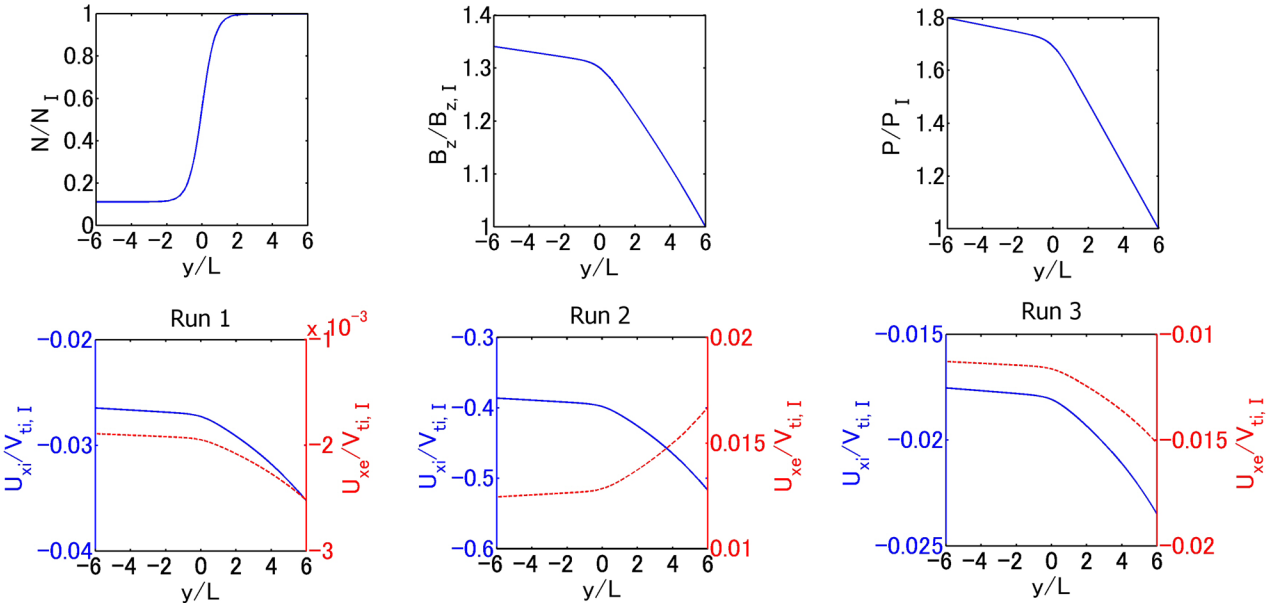

FIG. 1. Initial spatial profiles of the density N, the magnetic field B_z, the scalar pressure $P=(P_i+P_e)$, and the bulk velocity $U_{xi,e}$ as functions of y.

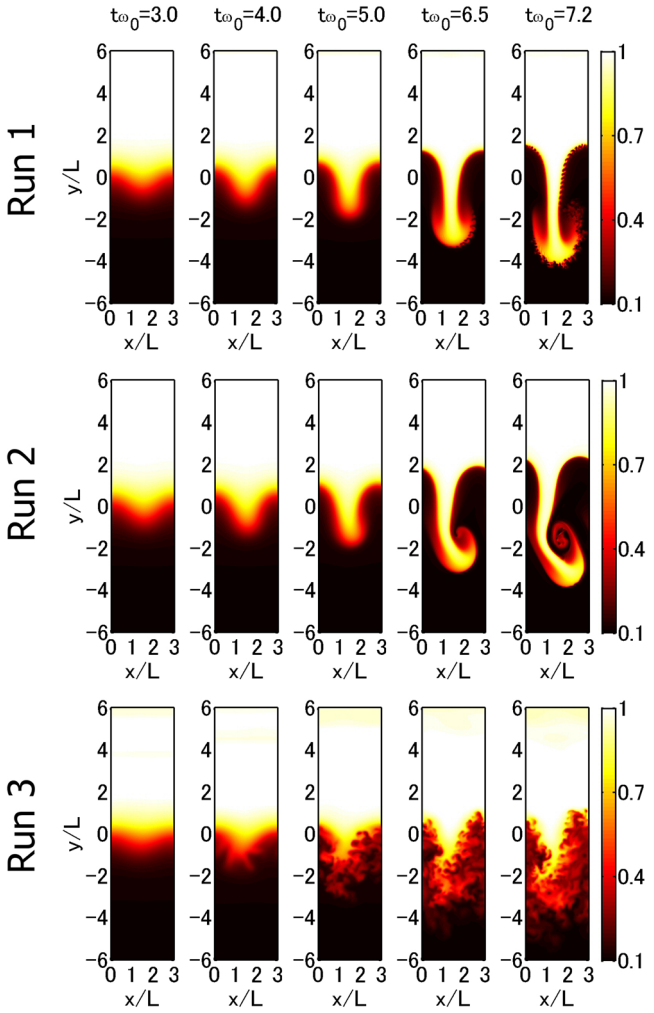

FIG. 2. Spatial profiles of ion density at different times in Runs 1 (top), 2 (middle), and 3 (bottom).

scale structures, however, do not disturb the nonlinear development of the RTI. The interchange of the high-density and low-density plasma continues as seen at $t\omega_0 = 7.2$ of Run 3 in Fig. 2.

Figure 3 shows the time history of the Fourier amplitude of the bulk velocity U_{iy} component at Mode 1 ($k_x L = 2.09$) in Runs 1–3. To obtain the spectral intensity in Fig. 3, we first Fourier-transform $U_{iy}(t, x, y)$ in the x direction and then integrate $U_{iy}(t, k_x, y)$ over $-0.83 \le y/L \le -0.77$ in which the MHD linear theory shows the maximum growth rate. The growth rate of Mode 1 calculated from the MHD linear theory is $\gamma \sim 0.827\omega_0$, which is shown by the dotted line. The spectral intensity is normalized by $L\omega_0$.

In Runs 1 and 2, the primary RTI grows at the MHD linear growth rate and saturates at $t\omega_0 \sim 5$. In Run 3, the primary RTI grows from the initial perturbation slightly smaller than that in Runs 1 and 2 (since the initial perturbation is given with respect to the Alfven velocity). The Fourier amplitude grows almost at the MHD linear growth rate but oscillates at the ion gyro frequency. The primary RTI saturates at $t\omega_0 \sim 4$ and then gradually grows through secondary (nonlinear) processes. The final Fourier amplitude of Mode 1 in Runs 1–3 is almost the same ($|U_y| \sim 10 L\omega_0$). Figures 2 and 3 show that the timescale for the growth of the RTI in Runs 1–3 is almost

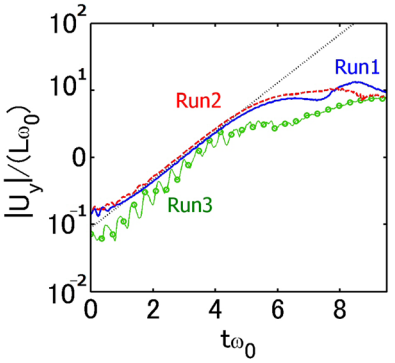

FIG. 3. Time history of the Fourier amplitude of the bulk velocity U_{iy} component at Mode 1 ($k_x L = 2.09$) in Runs 1–3. The normalization is with respect to $L\omega_0$. The theoretical MHD linear growth rate is shown by the dotted line.

the same, when the space and the time are normalized by L and ω_0, respectively. This also suggests that neither the Hall effect nor the ion gyro kinetic effect play roles in the linear growth of the primary RTI in Runs 1–3 (i.e., in the MHD regime), as described in Sec. II.

A. Hall effect in Run 2

To study mechanisms for the asymmetric development of the RTI in Run 2, we first analyze the electric field, especially the E_y component, which is a source of the ion convection in the x direction. We found that the electric field is expressed by the sum of the MHD term, the Hall term, and the pressure gradient term in Runs 1 and 2, i.e.,

$$\boldsymbol{E} \approx -\boldsymbol{U}_i \times \boldsymbol{B} + \frac{\boldsymbol{J} \times \boldsymbol{B}}{eN} - \frac{\nabla P_e}{eN}. \tag{14}$$

Note that the Ampere law ($\mu_0 \boldsymbol{J} = \nabla \times \boldsymbol{B}$) is well satisfied.

Figure 4 shows the electric field E_y component and its MHD, Hall, and electron pressure gradient terms at $t\omega_0 = 5$ in Runs 1 and 2. The MHD term is dominant in Run 1, while the Hall term is strongly enhanced at the right-hand side of the tip of the finger structure in Run 2. Note that the Hall term is small during the linear evolution in Run 2. The electron pressure gradient term is small in both Runs 1 and 2. The electric field E_y component in Run 1 is antisymmetric in the coordinate axis parallel to gravity, while electric field E_y component in Run 2 is asymmetric due to the strong Hall term. The result suggests that the motion of the tip of the finger structure in the $+x$ direction is caused by the Hall electric field.

We next analyze the bulk velocity. We found that the electron bulk velocity is expressed by the sum of the $\boldsymbol{E} \times \boldsymbol{B}$ drift, the diamagnetic drift, and the $\boldsymbol{g} \times \boldsymbol{B}$ drift in Runs 1 and 2, i.e.,

$$\boldsymbol{U}_e \approx \frac{\boldsymbol{E} \times \boldsymbol{B}}{|B|^2} + \frac{(\nabla P_e) \times \boldsymbol{B}}{eN_e |B|^2} - \frac{m_e \boldsymbol{g} \times \boldsymbol{B}}{e|B|^2}. \tag{15}$$

Noted that the stress terms in the electron pressure is very small (the pressure tensor is expressed as $\mathbf{P}_e \simeq P_e \mathbf{I}$ where $\mathbf{I}$ is the unit tensor), suggesting that the electron gyro kinetics is negligible. The ion bulk velocity, on the other hand, is expressed by the following equation:

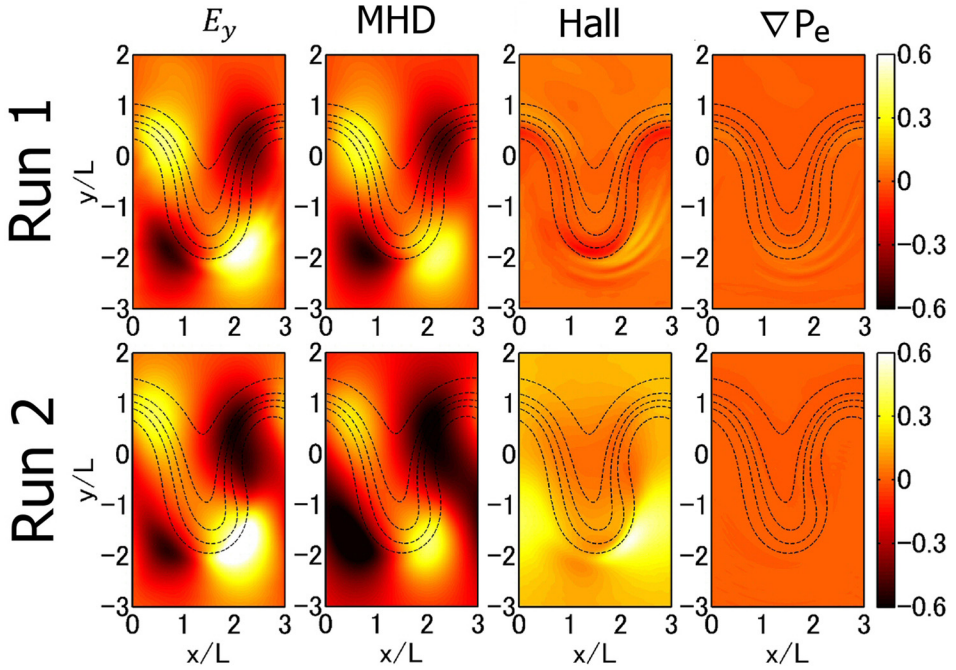

FIG. 4. Electric field E_y component and its MHD, Hall, and electron pressure gradient terms at $t\omega_0 = 5$ in Runs 1 (top) and 2 (bottom).

$$\boldsymbol{U}_i \approx \frac{(\boldsymbol{E}-\boldsymbol{E}_p)\times\boldsymbol{B}}{|B|^2} - \frac{(\nabla\cdot\mathbf{P}_i)\times\boldsymbol{B}}{eN_i|B|^2} + \frac{m_i\boldsymbol{g}\times\boldsymbol{B}}{e|B|^2}. \quad (16)$$

Here, $\boldsymbol{E}_p$ is the polarization electric field, which is almost zero in Run 1 but is non-zero in Run 2. It is noted that the polarization electric field is almost zero during the linear evolution but is enhanced after the saturation since $\mathrm{d}\boldsymbol{U}_i/\mathrm{d}t$ is finite due to the nonlinear development of the RT structure.

From Eqs. (15) and (16), we obtain the electric current density as

$$\boldsymbol{J} \approx -eN\frac{\boldsymbol{E}_p\times\boldsymbol{B}}{|B|^2} - \frac{(\nabla\cdot\mathbf{P})\times\boldsymbol{B}}{|B|^2} + (m_i+m_e)N\frac{\boldsymbol{g}\times\boldsymbol{B}}{|B|^2}. \quad (17)$$

The first term in the right-hand side is the polarization current ($\boldsymbol{J}_p$), the second term is the diamagnetic current ($\boldsymbol{J}_d$), and the third term is the current due to the $\boldsymbol{g}\times\boldsymbol{B}$ drift ($\boldsymbol{J}_g$).

Figure 5 shows the current density J_x component and its diamagnetic term, gravity term, and polarization term at $t\omega_0 = 5$ in Runs 1 and 2. In Run 1, the polarization term and the gravity term are small, and the diamagnetic current is most dominant. The electron component is dominant in the total diamagnetic current, which becomes a source of the electron-scale secondary KHI.[16]

In Run 2, the gravity term is stronger than in Run 1 and exists inside the contour line of the ion density. This term is also canceled out by the polarization current at the center of the finger structure. There also exists a strong negative

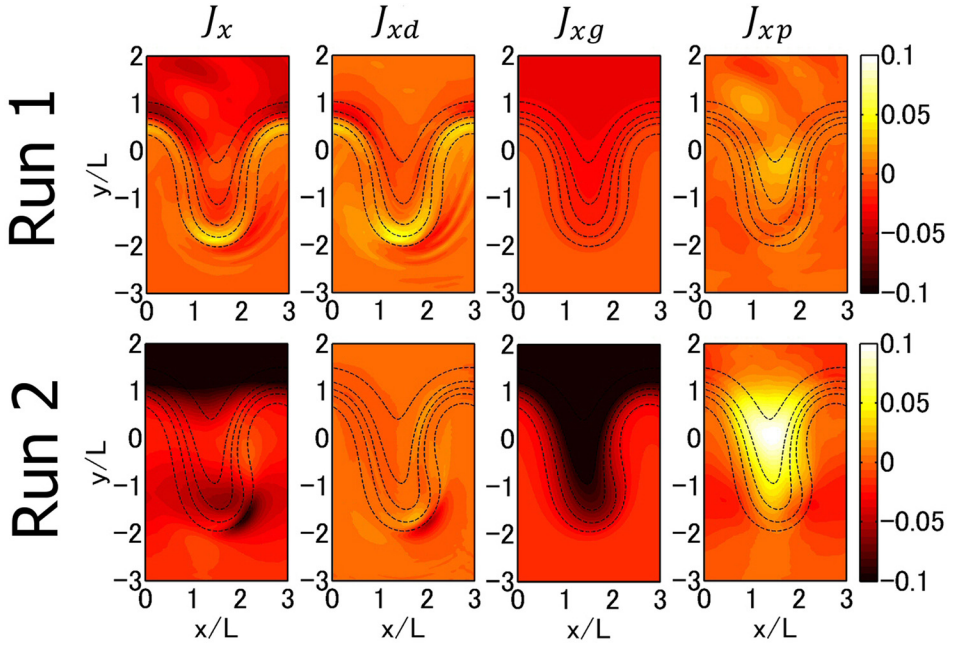

FIG. 5. Current density J_x component and its diamagnetic (J_{xd}), gravity (J_{xg}), and polarization (J_{xp}) terms at $t\omega_0 = 5$ in Runs 1 (top) and 2 (bottom).

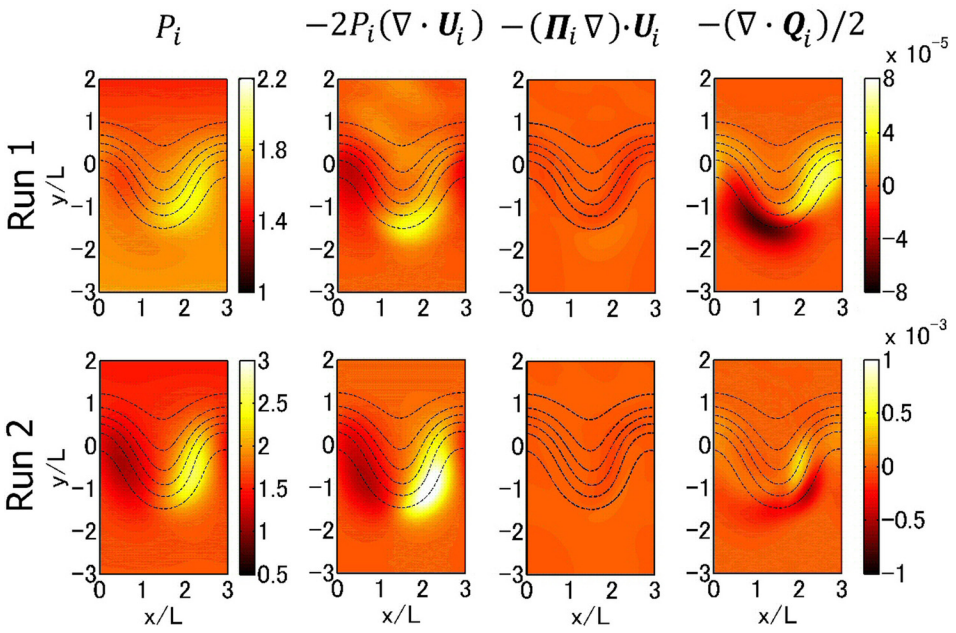

FIG. 6. Ion scalar pressure P_i and the corresponding compressible term, stress term, and heat flux term in the time-dependent scalar pressure equation at $t\omega_0 = 4$ in Runs 1 (top) and 2 (bottom).

diamagnetic current at the right-hand side of the tip of the finger structure (outside the contour line of the on density), which is due to the scalar pressure gradient of ions.

In both runs, the contribution of the stress term ($\boldsymbol{\Pi} \equiv \mathbf{P} - P\mathbf{I}$) is small, suggesting that the ion gyro kinetic effect is small in Runs 1 and 2. These results also suggest that the strong positive Hall electric field at the right-hand side of the tip of the finger structure in Run 2 (which is seen in Fig. 4) is generated by the ion diamagnetic current due to the scalar pressure gradient.

The time development of the scalar pressure is described by the following equation:

$$\frac{dP_i}{dt} = -\gamma P_i(\nabla\cdot\boldsymbol{U}_i) - (\gamma-1)(\boldsymbol{\Pi}_i\nabla)\cdot\boldsymbol{U}_i - \frac{\gamma-1}{2}\nabla\cdot\boldsymbol{Q}_i, \tag{18}$$

where $\gamma = 2$ in the present coordinate system. The first term in the right-hand side is the compressible term, the second term is the stress term, and the third term is the heat flux term (where $\boldsymbol{Q}_i \equiv (Q_{xxxi} + Q_{xyyi}, Q_{xxyi} + Q_{yyyi})$).

It is worth discussing the reason of the strong scalar pressure gradient seen in Run 2. Figure 6 shows the ion scalar pressure P_i and the corresponding compressible term, stress term, and heat flux term in the time-dependent scalar pressure equation at $t\omega_0 = 4$ in Runs 1 and 2. It is found that the stress term is negligible in both runs. It is also found that the structure of the ion scalar pressure is asymmetric in a coordinate axis parallel to gravity in both runs.

In Run 1, the enhancement of the ion scalar pressure gradient at the right-hand side of the finger structure becomes a source of the secondary electron-scale KHI.[16] Figure 6 clearly shows that the ion pressure at the right-hand side of the finger structure is enhanced by the both the compressible term and the heat flux term. In Run 2, on the other hand, the ion pressure at the right-hand side of the finger structure is enhanced by the compressible term rather than the heat flux term.

The ion bulk velocity, the ion pressure, and the magnetic field are modified by the Hall effect. However, these components cannot be separated into the MHD term and the Hall term as the electric field can be. Taking outer cross product of Eq. (17) and $\boldsymbol{B}$, we obtain

$$\boldsymbol{E}_{Hall} \approx \boldsymbol{E}_p + \frac{\nabla\cdot\mathbf{P}}{eN} - \frac{m_i+m_e}{e}\boldsymbol{g}. \tag{19}$$

In Fig. 4, we see a shear component in the Hall electric field E_{yHall} component at the right-hand side of the tip of the finger in Run 2. In Fig. 5, we see a compressible component in the polarization current J_{xp} component at the right-hand side of the tip of the finger in Run 2. From Eq. (19), it is suggested that the shear component of the Hall electric field is related to the polarization electric field and that the strong compressible flow in the bulk velocity U_x component is due to the Hall effect.

The structure of the vortex with counter-clockwise rotation seen in Run 2 (see Fig. 2) is similar to the structure of KH vortices. Figure 7 shows the structure of the secondary shear layer at the left-hand side and the right-hand side of the finger structure at $t\omega_0 = 5$ in Runs 1 and 2. We show the two-dimensional spatial profile of the ion density together with the definition of the coordinate axes taken in the directions normal and tangential to the density shear layer in the left panels. We also show the one-dimensional spatial profiles of the tangential ion velocity field U_ζ in the normal (ξ) direction in the right panels.

The half thickness of the secondary velocity shear layer formed by the primary RT at the right-hand side of the finger structure in Run 2 is obtained as $L_{Ui} \sim 0.22L$. Then, a typical wavelength of the KHI is estimated as $\lambda_{KH} \sim 4\pi L_{Ui} = 2.76L$. From Fig. 2, we estimate the spatial size of the vortex as $\lambda \sim 2.9L$, which is close to the wavelength of the KHI due to the secondary velocity shear.

In Run 1, the structure of the secondary velocity shear layer formed by the primary RTI is symmetric. This is why

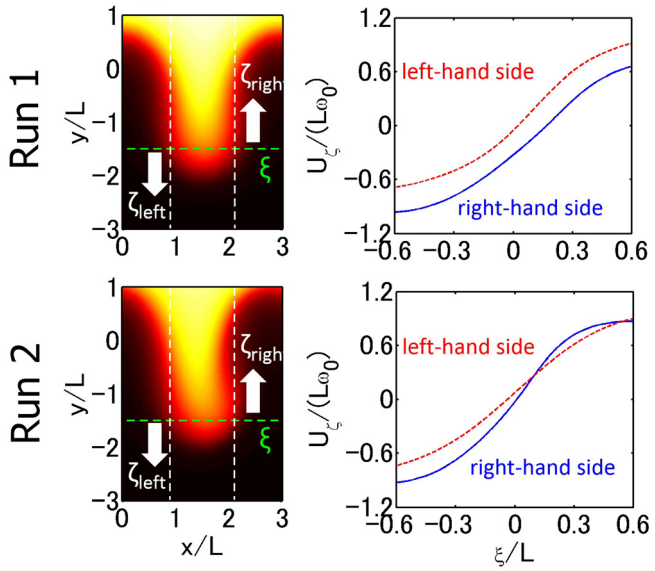

FIG. 7. Structure of the secondary shear layer at the left-hand side and the right-hand side of the finger structure at $t\omega_0 = 5$ in Runs 1 (top) and 2 (bottom). Two-dimensional spatial profile of the ion density together with the definition of the coordinate axes taken in the directions normal and tangential to the density shear layer is shown in the left panels. One-dimensional spatial profiles of the tangential ion velocity field U_ζ in the normal (ξ) direction are shown in the right panels.

ion-scale secondary KHIs are generated at both sides of the finger structure in the previous MHD simulations.[3–5] In Run 2, the structure of the secondary velocity shear layer is asymmetric. However, the magnitude of the velocity shear at the left-hand side of the finger structure is almost the same as that in Run 1. The magnitude of the velocity shear at the right-hand side of the finger structure is about twice as large as that at the left-hand side. This result suggests that the growth rate of the KHI due to the secondary velocity shear is on the same order, implying that there is a reason why the secondary KHI is enhanced only at the right-hand side of the finger structure in Run 2. Here, we propose that the motion of the tip of the finger structure in the $+x$ direction is enhanced by the Hall electric field, which becomes a seed perturbation of the secondary KHI.

B. Stress and heat flux effects in Run 3

In Run 3, a secondary perturbation with a spatial-scale smaller than the primary RTI is seen at $t\omega_0 = 4$. The structure of the ion density formed by the nonlinear development of the secondary perturbation is similar to that of the RTI, although there is no initial perturbation at the wavelength of

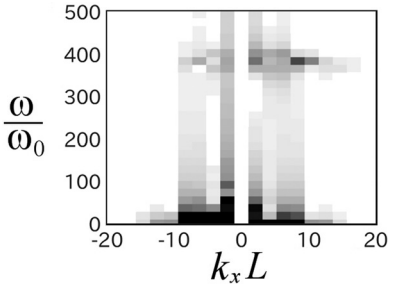

FIG. 9. Frequency-wavenumber spectrum of the current density J_{ey} component obtained by Fourier transformation of $J_y(t, x, y/L = -1)$ for $2.77 \le \omega_0 \le 3.11$ and $0 \le x/L \le 3$.

this perturbation. To investigate the origin of this perturbation, we show the current density J_y component together with the contour lines of the ion density N_i at $t\omega_0 = 2.8$, 3.2, and 3.6 in Fig. 8. Note that the Ampere law ($\mu_0 \boldsymbol{J} = \nabla \times \boldsymbol{B}$) is well satisfied. We found that there appears the perturbation in the current density J_y component from $t\omega_0 = 2.8$. The perturbation exists along a contour line of the ion density $N_i = 0.2N_I$, suggesting that the perturbation is excited below the density shear layer. The wavelength of the perturbation is estimated as $\lambda/L \sim 0.7 - 1$ (Modes 3 and 4).

Since there exists a strong pressure/temperature gradient at the location where the perturbation exists, it is expected that a secondary instability is generated by a diamagnetic current. The typical wavelength of the Lower-Hybrid Drift Instability (LHDI) is estimated as $\lambda_{LHD} \sim 2\pi\sqrt{r_i r_e}$.[23] The wavelength of the LHDI with the parameters (r_i and r_e) at $y/L \sim -1$ is obtained as $\lambda_{LHD} \sim 1.05L$, which is very close to the wavelength of the perturbation seen in Run 3. To see the frequency of the perturbation, we show the frequency-wavenumber spectrum of the current density J_{ey} component obtained by Fourier transformation of $J_y(t, x, y/L = -1)$ for $2.77 \le \omega_0 \le 3.11$ and $0 \le x/L \le 3$ in Fig. 9. The local ion cyclotron frequency and lower-hybrid resonance frequency at $y/L = -1$ are $\omega_{ci} = 15.5\omega_0$ and $\omega_{LHR} = 77.5\omega_0$, respectively. It is found that the frequency of the perturbation at Mode 4 ($k_x L = 8.38$) is close to the local electron cyclotron frequency $\omega \sim 375\omega_0 \sim \omega_{ce}$ at $y/L = -1$ rather than ω_{LHR}. It should be noted, however, that the phase velocity of these perturbations ($v_p \sim 48L\omega_0$) is too fast for the Landau resonance with the drifting ions ($U_{xi} \sim -0.16L\omega_0$). The direction of the phase velocity of the small-scale perturbations is opposite to the direction of the drift velocity of ions. These results suggest that the secondary instability does not correspond to the electron cyclotron drift instability nor the LHDI

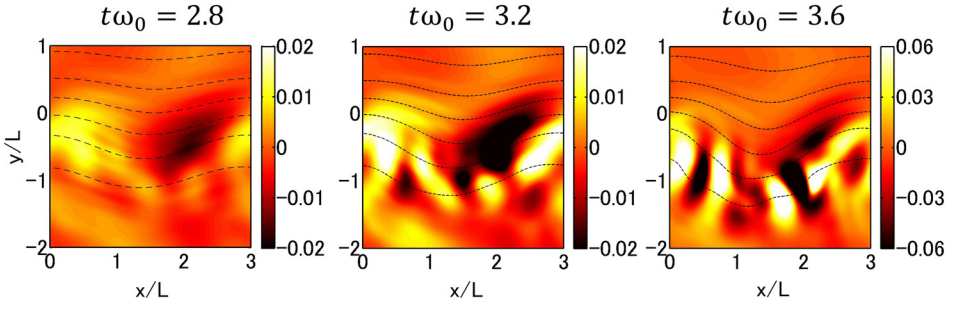

FIG. 8. Current density J_y component at different times in Run 3. The dashed lines show the contour lines of the ion density N_i.

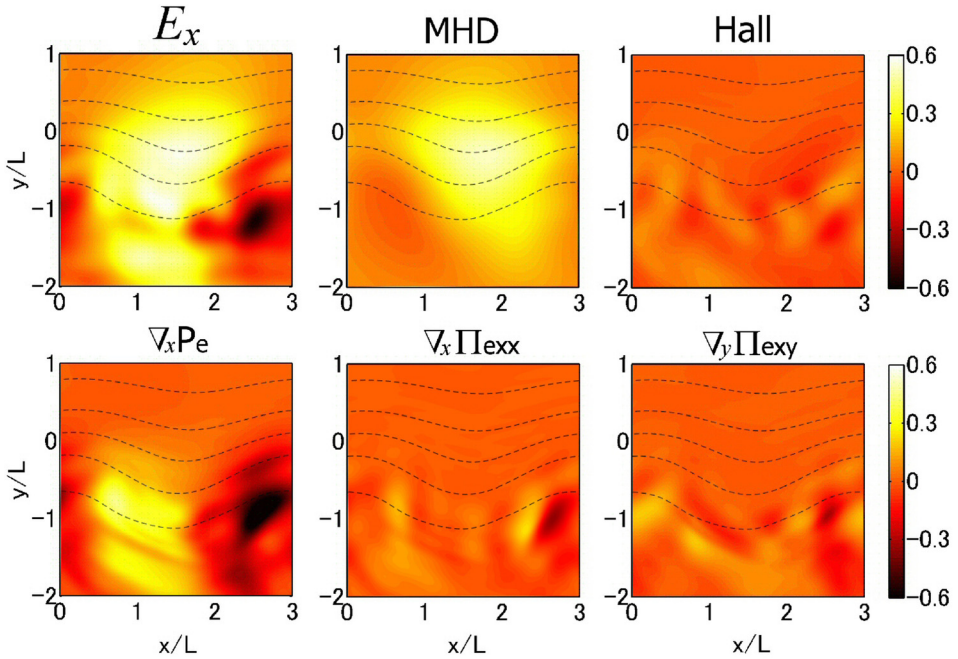

FIG. 10. Electric field E_y component and its MHD, Hall, electron scalar pressure gradient, and electron stress terms at $t\omega_0 = 3.2$ in Run 3.

due to the Landau resonance but is due to an ion anomalous cyclotron resonance $\omega - n\omega_{ci} = k_x U_{xi}$ with $n = 25$.

A recent three-dimensional full particle-in-cell simulation of magnetic reconnection has demonstrated that the LHDI is generated at the front of reconnection jets and that the LHDI becomes a seed perturbation of the secondary ballooning/interchange instability.[24] We propose a similar mechanism for the small-scale RTI as follows, although the generation mechanism of the secondary instability itself is still unclear. A perturbation of the velocity field with a short wavelength is excited by a secondary instability in the direction normal to the shear layer (in the direction parallel to the gravity). Then, the RTI with a short wavelength, which is linearly unstable but grows from the small initial perturbation, is enhanced by a new seed perturbation due to a secondary instability. The RTI with the short wavelength grows much faster than the secondary instability.

The plasma motion in the y direction is associated with the electric field E_x component. We separate the electric field into subcomponents based in Eq. (14) with the stress term. Figure 10 shows the electric field E_x component and its MHD, Hall, electron scalar pressure gradient, and electron stress terms at $t\omega_0 = 3.2$ in Run 3.

In contrast to Runs 1 and 2, the electron scalar pressure term has a larger contribution in Run 3. Both the electron stress terms also play roles in the electric field E_x component. It is clearly seen that the perturbation at Mode 4 appears in the Hall term and the stress terms, although the magnitudes of them are small at $t\omega_0 = 3.2$ due to the growth phase. It is not surprising that the Hall term plays a role in the small-

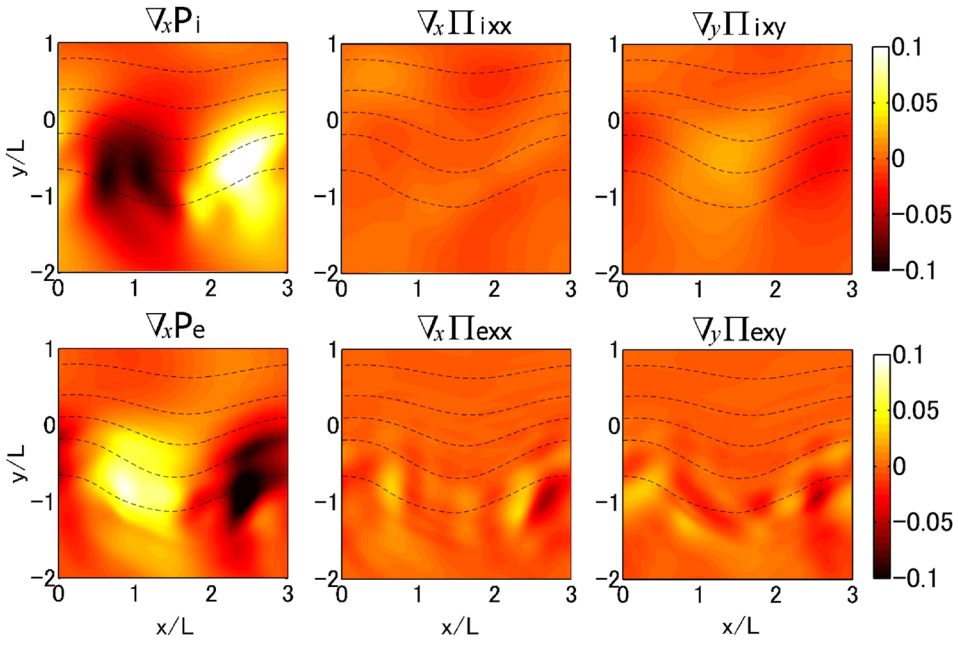

FIG. 11. The ion pressure gradient term $\partial P_i/\partial x$, the ion stress terms $\partial \Pi_{xxi}/\partial x$ and $\partial \Pi_{xyi}/\partial y$, the electron pressure gradient term $\partial P_e/\partial x$, the electron stress terms $\partial \Pi_{xxe}/\partial x$ and $\partial \Pi_{xye}/\partial y$ of the diamagnetic current J_{yd} component at $t\omega_0 = 3.2$ in Run 3.

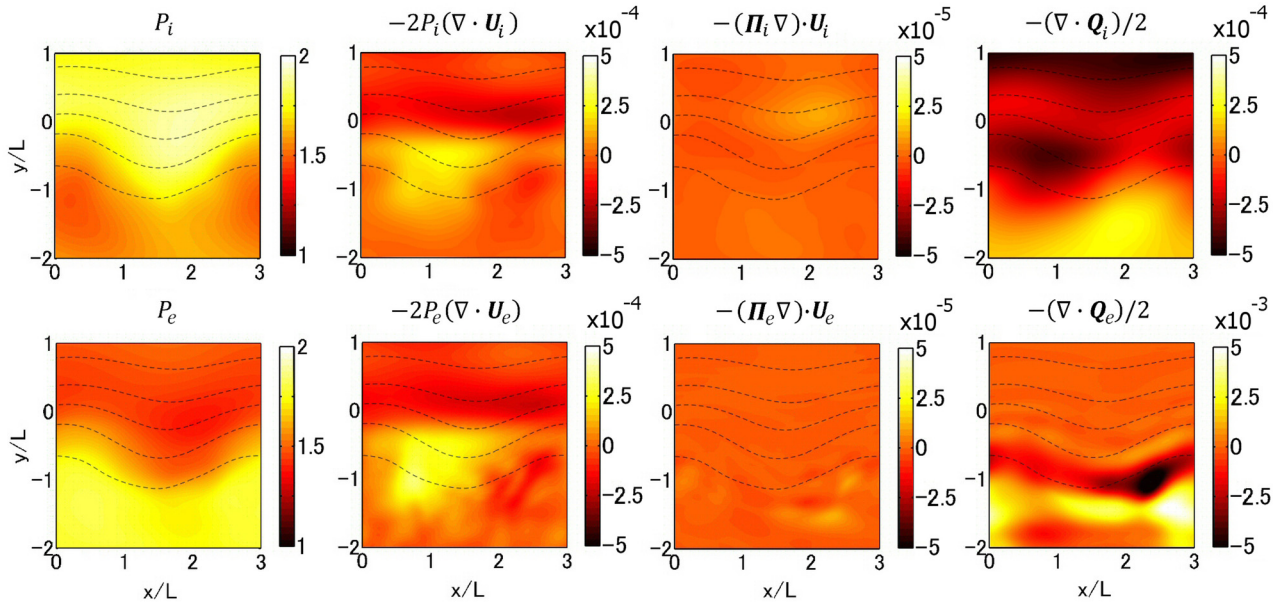

FIG. 12. Scalar pressure and the corresponding compressible term, stress term, and heat flux term in the time-dependent scalar pressure equation for ions (top) and electrons (bottom) at $t\omega_0 = 3.2$ in Run3.

scale perturbation since the wavelength is close to the ion inertial scale ($k_x d_i \sim 0.3$), although "ion gyro kinetic effects" were expected to play roles from the simulation parameters. In contrast to Run 2, however, the Hall term does not contribute to the nonlinear development of the primary RTI (Mode 1) but contribute to the growth of the small-scale perturbation by coupling with the electron stress terms. It is expected that the small-scale perturbation does not grow in Runs 1 and 2 since the electron stress term is negligible.

"What are ion gyro kinetic effects?" is an open question in plasma physics. In the present study, we discuss kinetic effects in terms of the stress tensor and the heat flux as differences from the standard fluid (MHD) equations. In Fig. 11, we separate the diamagnetic current J_{yd} component into the ion scalar pressure gradient, ion stress, electron scalar pressure gradient, and electron stress terms. It seems that the scalar pressure gradient terms are a majority component in the diamagnetic current J_{yd} component. However, the total scalar pressure gradient $\nabla(P_i + P_e)$ term has an amplitude almost equal to that of the electron stress terms at Mode 4. The small-scale perturbation is also supported by the electron stress terms $\partial\Pi_{xxe}/\partial x$ and $\partial\Pi_{xye}/\partial y$, as also seen in Fig. 10. Although the ion stress terms $\partial\Pi_{xxi}/\partial x$ and $\partial\Pi_{xyi}/\partial y$ are finite, their contributions are unexpectedly small.

Finally, we analyze the pressure equation (18) for both ions and electrons. Figure 12 shows the scalar pressure and the corresponding compressible term, stress term, and heat flux term in the time-dependent scalar pressure equation for ion and electrons at $t\omega_0 = 3.2$ in Run 3. Although the small-scale perturbation is not clear in each scalar pressure of ions and electrons in Fig. 12, the total scalar pressure $P_i + P_e$ has the perturbation at Mode 4. The perturbation at Mode 4 is also seen in the compressible terms of both ions and electrons. It is also found that both the ion and electron stress terms do not contribute to the time development of the scalar pressure, while both the ion and electron heat flux terms have a large contribution. The magnitude of the electron heat flux term is much larger than that of the other terms.

Although the "ion gyro kinetic" effect is expected to play a role in the nonlinear stage of Run 3, the present simulation result shows that the contribution of the ion stress terms is small. On the other hand, the electron stress terms unexpectedly play an important role in the excitation of a small-scale perturbation by coupling with the Hall electric field (i.e., electric current density/magnetic field). It is also shown that both the ion and electron heat flux terms have a large contribution to the time development of the scalar pressure. The present result suggests that the heat flux is not negligible for discussing the "gyro kinetics."

IV. CONCLUSIONS

A four-dimensional (two spatial dimensions and two velocity dimensions) Vlasov simulation is performed to study the non-MHD effects on nonlinear processes of the RTI. In order to distinguish the ion inertial (Hall) effect and the ion gyro kinetic effect, we performed three simulation runs with the different ratio of the wavelength of the primary RT mode λ_{RT} to the ion inertial length d_i or the ion gyro radius r_i by changing the plasma beta. In the run with $\lambda_{RT} \gg d_i$ and $\lambda_{RT} \gg r_i$, the RTI develops symmetrically in a coordinate axis parallel to gravity as seen in the previous MHD simulations.

In the run with $\lambda_{RT} \sim d_i$ and $\lambda_{RT} \gg r_i$, the RTI develops asymmetrically in a coordinate axis parallel to gravity. A compressible flow is formed at the secondary density shear layer by the Hall effect, which generates a strong scalar pressure gradient of ions. A Hall electric field is enhanced by the diamagnetic current due to the pressure gradient, which results in the asymmetric flow at the tip of the finger

structure. The strong velocity field due to the Hall effect enhances the ion-scale secondary KHI.

In the run with $\lambda_{RT} \gg d_i$ and $\lambda_{RT} \sim r_i$, a small-scale secondary RTI is excited at $k_x r_i \sim k_x d_i \sim 0.3$ around the saturation stage of the primary RTI. Electron scalar pressure and stress terms play roles in the electric field. It is shown that the electron stress term and the Hall term in the electric field are dominant in the growth of the small-scale perturbation, although the wavelength of the perturbation is much longer than the electron gyro radius. It is expected that the small-scale secondary RTI is generated from a seed perturbation excited by a pressure/temperature gradient driven secondary instability through an ion cyclotron resonance. However, the detailed analysis on the generation of the secondary instability is left as a future study. It is also found that the contributions of the ion stress tensor for the nonlinear development of the RTI are unexpectedly small, while the heat flux tensor plays a role in the development of the ion scalar pressure.

In conclusion, it is not easy to separate non-MHD effects into the inertial, gyro kinetic, and other effects by a single kinetic simulation, since the present simulation results suggest that the Hall effect couples with non-MHD stress tensors. Therefore, it is unclear whether the result of Run 2 is close to that of a Hall-MHD simulation. It is also unclear whether the result of Run 3 is close to that of an electron-ion two-fluid simulation with stress and heat flux tensors. Direct comparison of the present study with these fluid simulations is also left as a future study.

ACKNOWLEDGMENTS

This work was supported by MEXT/JSPS under Grant-In-Aid (KAKENHI) Nos. 25610144, 26287041, and 15K13572. The computer simulations were performed on the Fujitsu FX100 and CX400 supercomputer systems at Information Technology Center in Nagoya University, as a computational joint research program at the Institute for Space-Earth Environmental Research in Nagoya University and the HPCI Systems Research Projects (Nos. hp140064, hp150069, and hp160015).

[1]Y. Matsumoto and M. Hoshino, Geophys. Res. Lett. **31**, L02807, doi:10.1029/2003GL018195 (2004).
[2]Y. Matsumoto and M. Hoshino, J. Geophys. Res. **111**, A05213, doi:10.1029/2004JA010988 (2006).
[3]Y.-M. Wang and M. Nepveu, Astron. Astrophys. **118**, 267–274 (1983).
[4]B.-I. Jun, M. L. Norman, and J. M. Stone, Astrophys. J. **453**, 332–349 (1995).
[5]J. M. Stone and T. Gardiner, Phys. Fluids **19**, 094104 (2007).
[6]B. Srinivasan and X.-Z. Tang, Phys. Plasmas **19**, 082703 (2012).
[7]J. D. Huba, J. G. Lyon, and A. B. Hassam, Phys. Rev. Lett. **59**, 2971–2974 (1987).
[8]R. Goto, H. Miura, A. Ito, M. Sato, and T. Hatori, Plasma Fusion Res. **9**, 140376 (2014), available at http://www.jspf.or.jp/PFR/PFR_articles/pfr2014/pfr2014_09-1403076.html.
[9]R. Goto, H. Miura, A. Ito, M. Sato, and T. Hatori, Phys. Plasmas **22**, 032115 (2015).
[10]J. D. Huba, Phys. Plasmas **3**, 2523–2532 (1996).
[11]D. Winske, Phys. Plasmas **3**, 3966–3974 (1996).
[12]J. D. Huba and D. Winske, Phys. Plasmas **5**, 2305–2316 (1998).
[13]T. Umeda, J. Miwa, Y. Matsumoto, T. K. M. Nakamura, K. Togano, K. Fukazawa, and I. Shinohara, Phys. Plasmas **17**, 052311 (2010).
[14]T. Umeda, S. Ueno, and T. K. M. Nakamura, Plasma Phys. Controlled Fusion **56**, 075006 (2014).
[15]T. Umeda, N. Yamauchi, Y. Wada, and S. Ueno, Phys. Plasmas **23**, 054506 (2016).
[16]T. Umeda and Y. Wada, Phys. Plasmas **23**, 112117 (2016).
[17]T. Umeda, Earth, Planets Space **60**, 773–779 (2008).
[18]T. Umeda, Y. Nariyuki, and D. Kariya, Comput. Phys. Commun. **183**, 1094–1100 (2012).
[19]H. Schmitz and R. Grauer, Comput. Phys. Commun. **175**, 86–92 (2006).
[20]T. Umeda, K. Togano, and T. Ogino, Comput. Phys. Commun. **180**, 365–374 (2009).
[21]K. S. Yee, IEEE Trans. Antennas Propag. **14**, 302–0307 (1966).
[22]T. Umeda, K. Fukazawa, Y. Nariyuki, and T. Ogino, IEEE Trans. Plasma Sci. **40**, 1421–1428 (2012).
[23]W. Daughton, Phys. Plasmas **10**, 3103–3119 (2003).
[24]T. K. M. Nakamura, R. Nakamura, W. Baumjohann, T. Umeda, and I. Shinohara, Geophys. Res. Lett. **43**, 8356–8364, doi:10.1002/2016GL070215 (2016).